Simulation of a detector prototype with direct SiPM read-out and comparison with measurements

von

Andreas Künsken

Bachelorarbeit in Physik

vorgelegt der

Fakultät für Mathematik, Informatik und Naturwissenschaften

der Rheinisch-Westfälischen Technischen Hochschule Aachen

Juli 2010

Erstellt im

III. Physikalischen Institut A

Univ.-Prof. Dr. Thomas Hebbeker

Abstract

The features of a novel muon detection system are studied in this thesis with the help of GEANT4 simulations. The detector consists of a 10 cm×10 cm scintillator on whose top 3 mm×3 mm silicon photomultipliers are mounted. The scintillator may optionally be wrapped in a reflector. In the simulations various properties of the scintillator and the wrapping are varied like the scintillator thickness or the kind of wrapping and its reflectivity. Subsequently, the number of photons arriving at the SiPM is analyzed to determine the influence of the varied properties. Finally, the results of the simulations are compared to results that come from measurements with the detector setup.

Zusammenfassung

Die Eigenschaften eines neuen Myondetektionssystems werden in dieser Arbeit mit Hilfe von GEANT4-Simulationen untersucht. Der Detektor besteht aus einem 10 cm×10 cm Szintillator auf dessen Oberseite 3 mm×3 mm Silizumphotomultiplier angebracht sind. Der Szintillator kann zusätzlich in einen Reflektor eingewickelt werden. In den Simulationen werden verschiedene Merkmale des Szintillators und der Umhüllung variiert, wie zum Beispiel die Szintillatordicke oder die Umhüllung und ihre Reflektivität. Anschließend wird die Anzahl der Photonen am SiPM analysiert um den Einfluss der veränderten Merkmale zu bestimmen. Letztendlich werden die Ergebnisse der Simulation mit Ergebnissen von Messungen mit dem Detektoraufbau verglichen.

Contents

1 Introduction **1**

2 The LHC and the CMS detector **3**
2.1 LHC specifications . . . 3
2.2 CMS specifications . . . 3
2.3 The SLHC upgrade . . . 6

3 Muon detection **7**
3.1 Energy loss of particles in matter . . . 7
3.2 Scintillators . . . 8
3.2.1 Scintillation counters . . . 8
3.3 Semiconductors . . . 10
3.3.1 Diodes . . . 10
3.3.2 The avalanche photo diode . . . 11
3.3.3 The Geiger-mode APD . . . 12
3.3.4 Silicon photomultipliers . . . 12

4 Simulation setup **15**
4.1 The scintillator . . . 15
4.2 The SiPM . . . 17
4.3 The setup . . . 17
4.4 The simulation parameter . . . 18

5 Comparison of simulation and measurement **21**
5.1 Simulation results . . . 21
5.1.1 Photon distribution on the SiPM . . . 30
5.2 Comparison with measurements . . . 30

6 Conclusion and Outlook **33**

A 3D photon distribution **35**

List of Figures

2.1 LHC overview [LHC10] . . . 4
2.2 CMS cross section [CMS10b] . . . 5
2.3 Muon Track fast Tag [Mon07] . . . 6

3.1 Energy loss of muons in matter [Gro08] . . . 7
3.2 Scintillation process . . . 9
3.3 Energy bands in a doped semiconductor . . . 11
3.4 SiPM noise . . . 13

4.1 Simulated and real SiPM . . . 16
4.2 Spectra of the scintillator and the SiPM [Bic10],[Ham08]. . . . 16
4.3 Temperature fluctuations at the test stand [Sch10] . . . 17
4.4 Simulated muon passage . . . 20

5.1 Photon number and cut stages . . . 21
5.2 Fit to the surface roughness . . . 24
5.3 MPVs for cut stages and ratio . . . 25
5.4 Photon threshold analysis . . . 27
5.5 Photon distribution on the SiPM . . . 31
5.6 Simulation and measurement MPVs . . . 32

6.1 Results for the scintillators . . . 34

A.1 3D photon distribution on 6mm and 8mm scintillator . . . 36

List of Tables

4.1 SiPM properties 18
4.2 Complete list of simulated setups. 19

5.1 MPV ratio for detect photons and photons at the SiPM 23
5.2 Ratio of the photon number for 8 mm and 6 mm scintillator 26
5.3 Fractions of events below photon thresholds for 8 mm scintillator . 28
5.4 Fractions of events below photon thresholds for 6 mm scintillator . 29
5.5 Fractions of events below photon thresholds without reflector. . . . 29

1 Introduction

In the past, particle collision experiments have proven concepts of theoretical physics. Several particles could be observed with the help of particle colliders like for example the detection of the top quark [CDF95], W-bosons, Z-bosons and many others. But to look even deeper into the microcosm of matter it is inevitable to reach higher collision energies and thus to gain a higher resolution of subatomic structures. With the LHC[1] it became possible to take a look at the interactions that keep our world together. The collision energy that is available with the LHC makes it possible to restore conditions that are similar to those fractions of seconds after the big bang. An aim of the LHC is to find evidence for the existence of the Higgs boson as well as to search for new physics. If the detectors at the LHC successfully reconstructed evidence for the Higgs or new physics, it would be a great achievement. But to detect this, efficient trigger systems are necessary. Especially a reliable muon system is required for Higgs detection to detect the *Golden Channel*

$$\mathrm{pp} \rightarrow \mathrm{H} \rightarrow \mathrm{ZZ}^{(*)} \rightarrow 4\mu. \tag{1.1}$$

A possible upgrade of the LHC to SLHC[2] as it is announced [Gia05] for the future (see chapter 2.3) requires also an upgrade of the muon system. For this update a new type of detector has been proposed [Mon07]. The features of a possible setup are studied in the scope of this thesis. This is done in cooperation with [Sch10].

[1] **L**arge **H**adron **C**ollider
[2] **S**uper **L**arge **H**adron **C**ollider

2 The LHC and the CMS detector

2.1 LHC specifications

The LHC is a particle accelerator located at CERN in Geneva, Swizerland and was constructed as a proton-proton collider ring [Eva08]. It is built 45 m to 170 m underground with a circumference of approximately 27 km. In 2009 it has been taken into operation and by now collisions at 7 TeV center-of-mass energy have been performed successfully, which is for now the highest center-of-mass energy ever reached in a particle collision experiment. The aim is to achieve collisions at 14 TeV in further runs. Around the LHC there are 4 main particle collision experiments (see figure 2.1), namely ALICE[1], ATLAS[2], LHCb[3] and CMS[4].
A physical quantity to describe the performance of an accelerator is its luminosity $\mathcal{L}$. It is defined as:

$$\mathcal{L} = f \cdot \frac{n_b N_1 N_2}{4\pi\sigma_x\sigma_y}, \tag{2.1}$$

where f is the revolution frequency of the bunches, N_1 and N_2 the number of bunches per beam, n_b the amount of particles per bunch and σ_x and σ_y the spatial extents of the beams at the interaction point. The momentary design peak luminosity of LHC is $10^{34}\frac{1}{\mathrm{cm}^2\mathrm{s}}$ which will be reached in the coming months. At design luminosity, the bunches cross every 25 ns and the collision rate is at 1 GHz, when assuming a proton cross section of 100 mb. To resolve these events, a fast detection system is needed.

2.2 CMS specifications

The CMS is a cylindrical particle detector at the LHC in Cessy, France. It has a diameter of 14.6 m, a total weight of about 12500 t and its length values to 21.6 m [CMS10a]. CMS was mostly built on the surface, it consists of 5 wheels and 2 end caps that were lowered underground and then mounted again. The particle detection system of CMS is composed of basically four layers of which the innermost is the tracker using pixel detectors and silicon strip detectors to

[1] **A** **L**arge **I**on **C**ollider **E**xperiment
[2] **A** **T**oroidal **L**HC **A**pparatu**S**
[3] **L**arge **H**adron **C**ollider **b**eauty
[4] **C**ompact **M**uon **S**olenoid

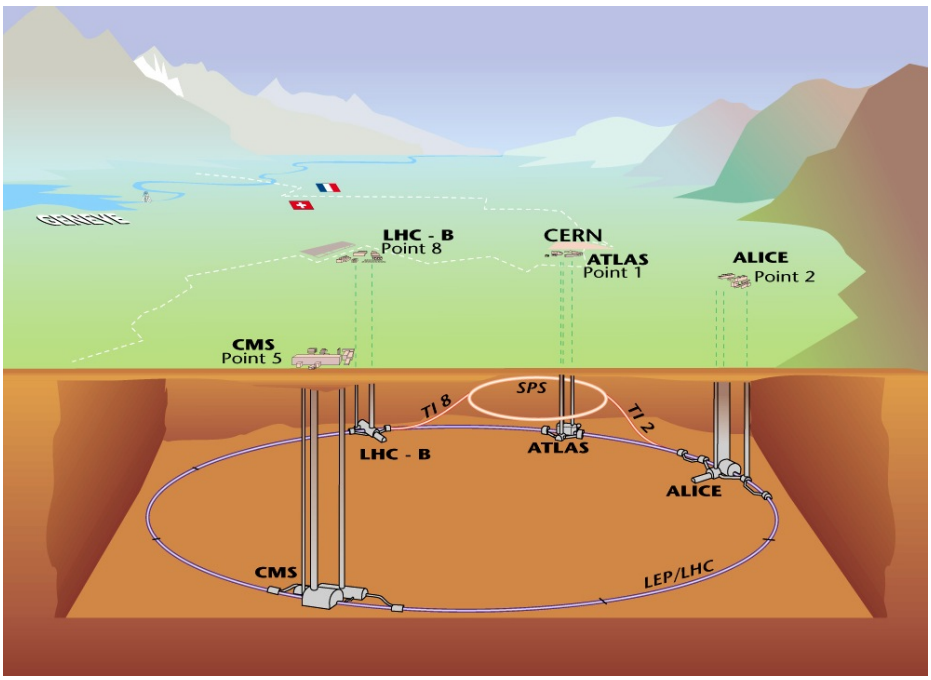

Figure 2.1: Schematic overall view of the LHC with its 4 main experiments.

determine the trajectories of charged particles, which were created in a collision. The next layer is the ECAL[5]. It is built of lead tungstate crystals, which are used to determine the energy of incoming photons and electrons. The third layer is the HCAL[6] which is used for detecting hadrons and measuring their energy. It is made of alternating layers of absorber material and scintillating material. As the cross section of muons in matter is small, the outermost layer of CMS is the muon detection system because muons, in contrast to other particles, pass the whole detector. To detect the muons, the system uses drift tubes and cathode strip chambers. Drift tubes consist of a cylindrical cathode along whose axis of symmetry an anode wire is drawn. The inner volume is filled with gas. Passing particles induce charges. While these charges drift towards the wire and the cylinder, new electron-ion pairs are created and the resulting current pulse can be measured at the end of the wires. The cathode strip chamber's working principle is the same as that of the drift tubes but they have a different geometry. Here the cathodes form an array of conducting strips above which a lattice of anode wires is clamped perpendicularly.

[5]**e**lectromagnetic **cal**orimeter
[6]**h**adronic **cal**orimeter

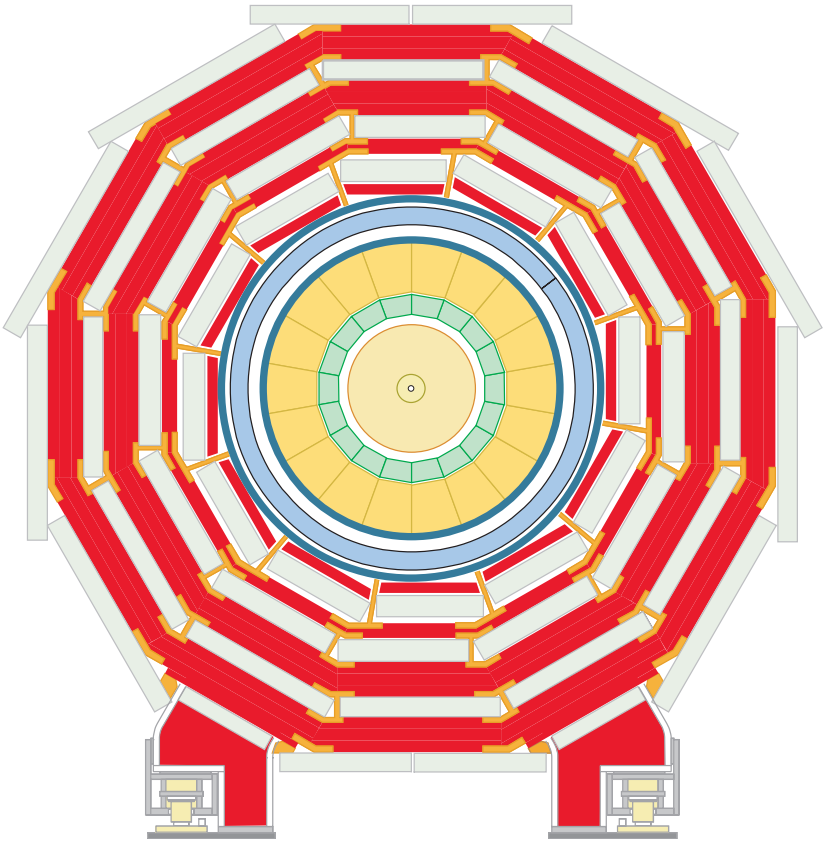

Figure 2.2: Cross section of the CMS detector in ϕ-plane. The inner yellow ring is the tracker, green is the ECAL, the outer yellow ring is the HCAL, blue is the magnet, grey is the muon system. Red are the parts of the iron flux return yoke.

An important part of the detector is a solenoidal magnet, which is used to deflect the charged particles from their initial trajectory with the help of the Lorentz force $\boldsymbol{F} = q(\boldsymbol{v} \times \boldsymbol{B})$. Because of the large energy and momentum of the emerging particles a strong magnetic field is required to achieve the required bending power. The necessary magnetic field may be calculated by $\mathrm{B} = \frac{\mathrm{p_T}}{0.3 \cdot \rho}$ where $\mathrm{p_T}$ is the transverse momentum in GeV and ρ is the bending radius of the trajectory. The applied field is at about 4 T.
The magnetic field and the highly ionizing radiation have great influence on the read-out electronics and may interfere with small signal currents. To weaken the impact on the created signals they need to be amplified very early.

2.3 The SLHC upgrade

To gain an even higher luminosity an upgrade of the LHC to SLHC is already planned due to which the luminosity of the accelerator shall be increased by one order of magnitude to $10^{35}\frac{1}{\mathrm{cm}^2\mathrm{s}}$ [Gia05]. By this the rate of collisions will be increased, which improves the search for new physics and rises the Higgs production rate. The shutdown phase of the accelerator is planned to be used for a CMS upgrade. In the scope of this thesis especially the upgrade of the muon system is of interest. A system called *Muon Track fast Tag* (MTT) has been proposed that would be able to trigger on muon passages and narrow the area for muon detection in the Tracker [Mon07]. This results in a better measurement of the transverse muon momentum due to the invocation of the Tracker in an early triggering stage. It is planned to place the MTT behind the solenoid (in the r-ϕ plane, see figure 2.3). For this, the MTT needs to be small to fit in that place, which will be realized with detector modules of a size in orders of magnitude from 10 cm×10 cm to 25 cm×25 cm and a height in the order of magnitude of 1 cm. Another requirement for the detector is that it needs to be fast because the expected event rate per area is approximately $1\ \frac{\mathrm{Hz}}{\mathrm{cm}^2}$.

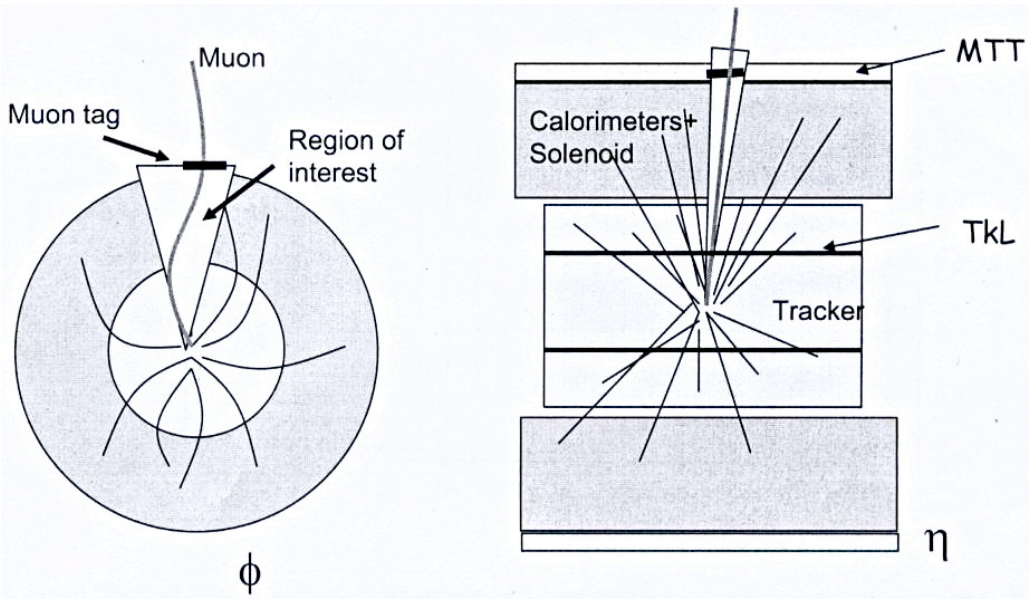

Figure 2.3: Schematic of the planned MTT position in ϕ- and η-plane, respectively.

3 Muon detection

3.1 Energy loss of particles in matter

A particle that passes matter looses energy by interacting with it. The loss of energy follows the Bethe-Bloch formula [Mar06] see figure 3.1 and is defined as $\frac{dE}{dx}$, the energy loss per path length. From the Bethe-Bloch formula follows that in the region of interest the released energy is linearly dependent of the distance the particle travelled in matter, which plays an important role for the detector setup. The means of detecting muons with the help of their released energy is explained in the following.

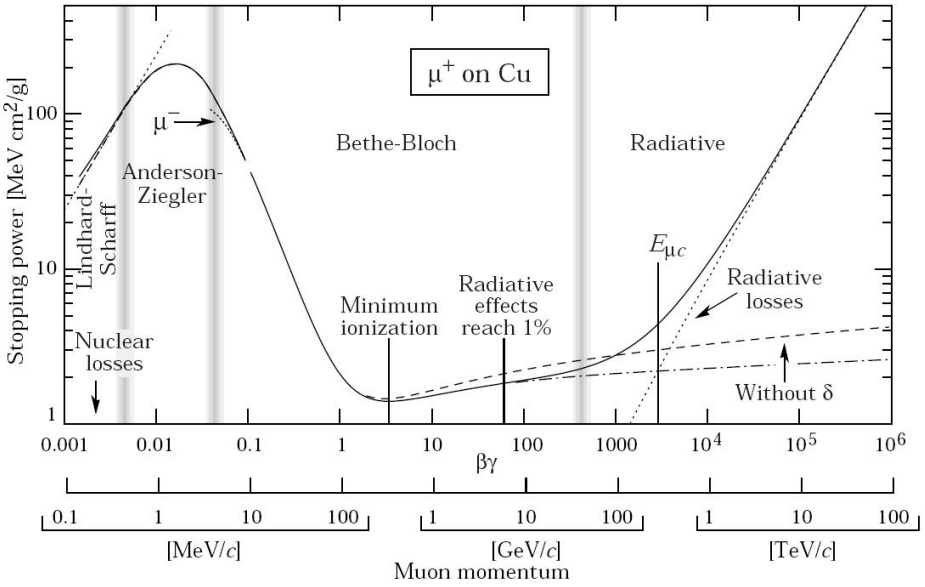

Figure 3.1: Energy loss of muons in matter. In the scope of this thesis, the part from 1 GeV to 1000 GeV muon energy is the relevant one.

3.2 Scintillators

Scintillation[1] is a certain type of luminescence — the emission of light after absorption of energy. There are two major types of scintillators, the organic scintillators and the inorganic scintillators, each of which has advantages and disadvantages. On the one hand the organic scintillators (e.g. plastic, anthracene) have the advantage of being unexpensive, arbitrary shapeable and fast at emission of photons after excitation (in the order of magnitude of some nanoseconds [Gru08]). Disadvantages are a comparably poor energy resolution and susceptibility to damages done by radiation. On the other hand the inorganic scintillators have a better energy resolution but are rather expensive, hard to get in the desired shape and also susceptible to radiation damage. Additionally, the light yield of inorganic scintillators is not as good as that of organic scintillators.
Scintillation occurs after excitation of the scintillating material by charged particles or γ-rays. An organic scintillator was used in the scope of this thesis. The scintillation progress in it works as follows (see fig. 3.2).
When a particle passes the scintillator, the electrons of its molecules may be lifted to a higher energy level. Within some picoseconds, the electrons decrease their excitation level via non-radiating transitions within the molecule (e.g. vibrations, collisions $\rightarrow$ phonons). Finally, the electrons emit photons when falling back into their initial state. The energy necessary to excite a molecule of an organic scintillator is in the order of magnitude of some electron volts. Yet the mean energy that is required to create a scintillation photon is approximately 100 eV [Gro08] since the incident radiation does not necessarily have to lift an electron but may also cause the excitation of phonons. As the excitation energies for the electrons slightly differ for every scintillator, each scintillator has its own emission spectrum. This plays an important role when selecting a scintillator for an experiment, because the photomultipliers connected to the scintillator should be most sensitive to the peak of the emitted scintillator spectrum.

3.2.1 Scintillation counters

A scintillation counter (compare [Gru08]) is used to convert emitted photons of the scintillator into electric signals, which may be processed by some read-out electronics. A common type of scintillation counter has a light guide mounted on the scintillator which leads the created photons to a photomultiplier tube (PMT). This type of scintillation counter is used in the setup to generate a trigger for muon detection. Another way to realize photomultipliers is on semi conductor base (see chapter 3.3). These photomultipliers require less space and their operating voltage is smaller compared to PMTs but they still may reach a gain comparable to a PMT.

[1] from Latin scintillare: twinkle, flare

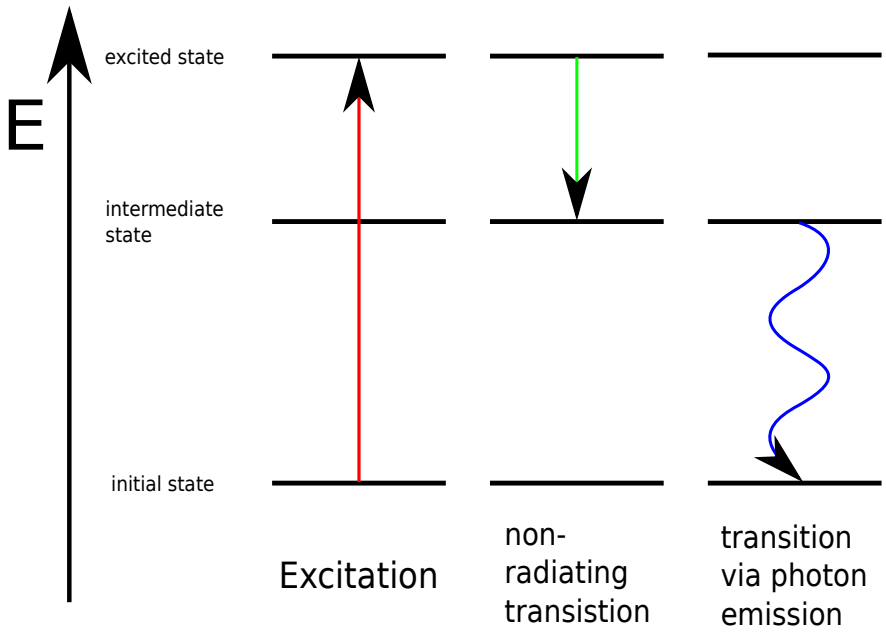

Figure 3.2: The scintillation process with focuses on the energy states.

The detector that is focused on in this thesis is designed as a scintillation counter which uses semi conductor photomultipliers.

3.3 Semiconductors

A good way to explain semiconductors is the notion of energy bands for the possible states of the electrons in the semiconductor. The bands that are important to explain the processes in the detector are the conductive band and the valence band. Materials are subdivided into three different types regarding their conductivity. The first type is the conductors, which conduct currents well because the conductive and the valence band overlap. The second is the semiconductors. Their bands do not overlap but have a so called band gap that is on the order of magnitude of 1 eV. The last type is the insulators whose band gap is at least 10 eV [Ser05]. The larger the band gap the more difficult it is to lift electrons from the valence band to the conductive band and the worse is the material's conductivity.

3.3.1 Diodes

A way to increase the conductivity of semiconductors is to bring in impurities into its crystal lattice referred to as doping. These impurities are usually foreign atoms which have either an electron more or an electron less in the valence band compared to the semiconductor's atoms. An additional electron in the foreign atom creates a donor level close to the conductive band from which the electrons may be lifted easily into the conductive band. As a result the conductivity is increased because the electrons may now move freely through the crystal lattice in the conductive band. A missing electron, called hole, creates an acceptor level close to the valence band to which electrons of the valence band may be excited so that the hole may also move freely in the valence band. A semiconductor with an additional acceptor level is called p-doped, if it has an additional donor level it is called n-doped. In general, a silicon semiconductor detector is based on p-doped and n-doped silicon. A junction of p- and n-doped material causes the Fermi energies, which are initially different for the p- and n-doped silicon, to align (see figure 3.3). This results in a shift of the conductive and the valence band in the region of the junction creating a potential that causes the holes and electrons close to the junction to recombine. Thus a charge-carrier-free zone called depletion layer develops around the junction. This device is known as a diode. Usually the doping in semiconductor detectors is asymmetrical with more electrons than holes and the p-doped area is smaller than the n-doped one. This is done to keep the detection process controllable (see chapter 3.3.3).

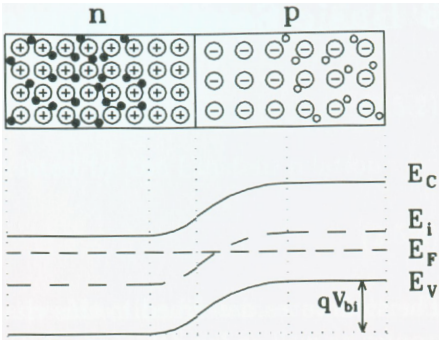

(a) Energy bands in doped semiconductor without pn-junction

(b) Energy bands in doped semiconductor with pn-junction

Figure 3.3: Configuration of the energy bands in a semiconductor [Lut07].

3.3.2 The avalanche photo diode

To create an APD[2] (see also [Ren09]), the diode described in the preceding chapter is now put on reverse bias voltage, which extends the depletion layer. This is important because the depletion layer is the sensitive volume for photon detection, and by broadening it the probability for photon detection increases. Photons passing the volume are absorbed and create an electron-hole pair. This is then split and electron and hole are drawn to the electrodes, respectively. Due to the high electric field in the APD, the electrons create further electron-hole pairs on their way to the electrodes, which results in an avalanche. In APDs the holes do not contribute to the avalanche by creating electron-hole pairs themselves because this would make the detection current incontrollable. The thickness of the depletion layer is an important quantity. Therefore it is useful to calculate its width by (see [Gro08])

$$w = \sqrt{2\epsilon(\mathrm{V} - \mathrm{V}_{\mathrm{bias}})/Ne} \tag{3.1}$$

where ϵ is the dielectric constant of the semiconductor, $\mathrm{V}_{\mathrm{bias}}$ the applied bias voltage, V the internal bias voltage, which denotes the potential caused by the band shift, N the doping concentration and e the electronic charge. In this formula the assumption was made that the doping is asymmetrical and thus N denotes the concentration of the higher doped material.

[2] **a**valanche **p**hoto **d**iode

3.3.3 The Geiger-mode APD

A G-APD[3] is a special type of APDs (compare [Ren09]). While the signal from APDs responds nearly linearly to the incoming light signal, G-APDs will always give away the same charge when being triggered. This happens because the bias voltage for the G-APDs, which is in the order of 100 V, makes the diode work in the so called Geiger-mode giving the diode its name. In this mode the avalanche effect reaches its maximum and a single photon may cause an avalanche due to the high electric field inside the G-APD. Therefore it is possible to detect minimal photon fluxes and even the number of detected photons may be calculated as the yielded charge is always the same. The current evolving in an avalanche would destroy the G-APD without a quenching mechanism. To quench the current a small resistor is placed on one side of the G-APD. Also holes may contribute to the avalanche effect which makes it even more difficult to quench the current. Thus the p-doped area is kept small to restrict the contribution of holes to the avalanche. The necessary time to gather the charge in a pixel is about 30 ns [Gru08], which makes the pixel detector useful for experiments where particles are expected to hit the detector with high frequencies. However, it is important to note that also some time to restore the depletion layer is necessary and the required time to process the information may be longer.

3.3.4 Silicon photomultipliers

A silicon photomultiplier (SiPM) is a pixel detector that consists of an array of usually quadratic G-APDs with an edge length in the order of magnitude of 10 µm to 100 µm. A feature of SiPMs, which has to be considered is the photon detection efficiency (PDE). This quantity is defined as [Ham08]

$$\mathrm{PDE} = \mathrm{Q_E} \times \mathcal{F} \times \mathrm{P_A}. \tag{3.2}$$

$\mathrm{Q_E}$ denotes the quantum efficiency, the number of generated electron-hole pairs divided by the number of incident photons. $\mathcal{F}$ is called the fill factor. It is defined as the ratio of the sensitive area A_{sens} and the total area A_{tot} of a single pixel:

$$\mathcal{F} = \frac{\mathrm{A}_{sens}}{\mathrm{A}_{tot}}. \tag{3.3}$$

This is due to the fact that the pixels need separations not to form a single big pixel and the connection to the voltage supply and the quenching resistors also require some space. Eventually $\mathrm{P_A}$ is the probability that an incident photon starts an avalanche. The PDE is a wavelength dependent quantity and should peak at the expected photon wavelength.

[3] **G**eiger-mode **a**valanche **p**hoto **d**iode

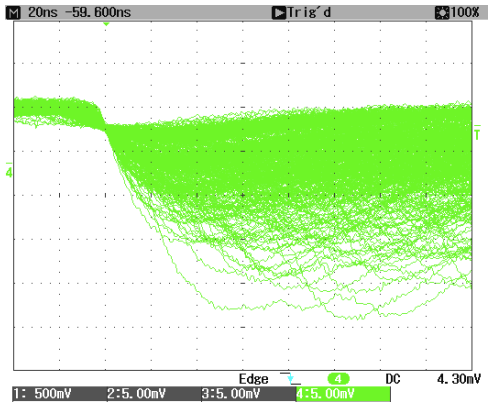

(a) Signal of an SiPM at ≈ 30 °C. No discrete pulses are visible.

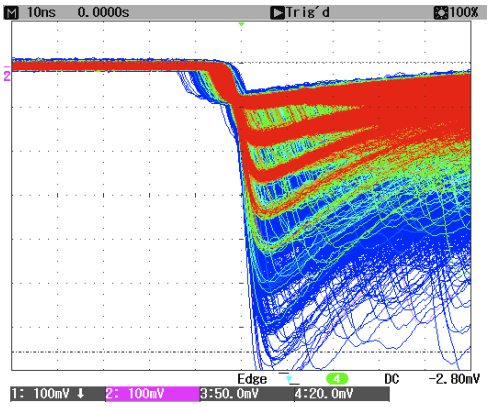

(b) Signal of an SiPM operated at the correct temperature. The different photon stages are clearly visible. (Picture taken with a 1 mm×1 mm SiPM.)

Figure 3.4: Images of the SiPM signals for each a properly working one and a too hot one.

SiPM side effects

It may happen that an electron is moved out of its atomic shell by thermal excitation. If this happens in the charge carrier free zone, the electron may start an avalanche that will make the detector create a signal, although no photon has passed. This is known as the noise of the SiPM or dark count rate and depends on the applied bias voltage and the temperature of the device. Both have been observed during measurements (see figure 3.4). Therefore it is necessary to provide the SiPM with a stable bias voltage and a constant temperature to keep the SiPM noise on a constant level.
An effect that affects the precision of determining the number of photons that were detected is optical cross-talk. This happens when in the run of an avalanche new photons are created that are then detected in other pixels. Hereby the number of measured photons may be higher than the actual number of incident photons.
Another side effect is the so called afterpulsing. Here charge carriers get trapped in the crystal lattice and come free with some delay. The carriers may then induce a second avalanche and cause deviations in the measured photon number from the true incident photon number (see also [Ham08]).

4 Simulation setup

The simulation of the detector is based on the GEANT4[1] framework. GEANT4 is a C++ toolkit from CERN to simulate the passage of particles through matter. For this purpose it provides a variety of interactions that may be included modularly into the simulation. The first step of a simulation is to create objects corresponding to the components of the detector. These so called *Solids* contain information about the object's geometry. Then a *LogicalVolume* is needed to store information about the material in the *Solid*. Additionally the volumes may be marked as sensitive volumes to generate *Hits* when a particle passes. These *Hits* provide functions for the user to gain information about the event when the sensitive volume was hit. Finally the *PhysicalVolume* is created. This is the complete volume used for the simulation [GEA10]. An existing simulation [Pap10] has been extended because the original program was capable of simulating SiPMs with only 100 pixels and now accepts various amounts of pixels. The only restriction is that the number of pixels needs to be a square number. An image of the SiPM and its simulation setup is given in figure 4.1.

4.1 The scintillator

In the scope of the simulations two sizes of the scintillator were used:

- A 100 mm×100 mm×8 mm scintillator.
- A 100 mm×100 mm×6 mm scintillator.

Scintillation photons are created uniformly in the solid angle and propagate arbitrarily through the scintillator. When they hit the surface of the scintillator on the inner side a part of the photons is reflected due to total internal reflection. To increase the number of scintillation photons that hit the SiPM the scintillator is wrapped in reflecting material because otherwise the photons that are being refracted would be lost. The reflectors used are a diffuse and a specular reflector, but to estimate the increase of detected photons when using a reflector measurements are taken with a scintillator wrapped in black felt. Small holes in the shape of the SiPM were cut into the wrappings to place the SiPM on the scintillator. The emitted spectrum of the scintillator is shown in figure (4.2(a)). The manufacturer states the peak of the emission spectrum to be at 408 nm (see [Gob]).

[1] **Ge**ometry **A**nd **T**racking

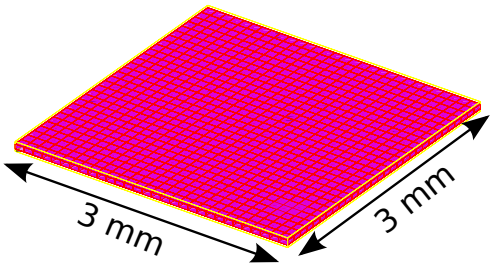

(a) Representation of the simulated SiPM. Pink is the sensitive area. The red lines in between are the non-sensitive SiPM material.

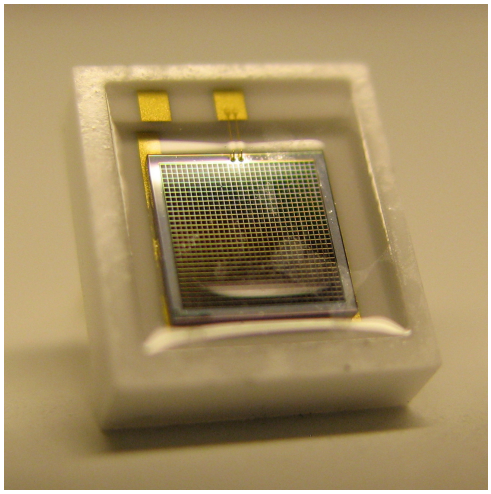

(b) Image of a real SiPM

Figure 4.1: Images of both the simulated and the real SiPM.

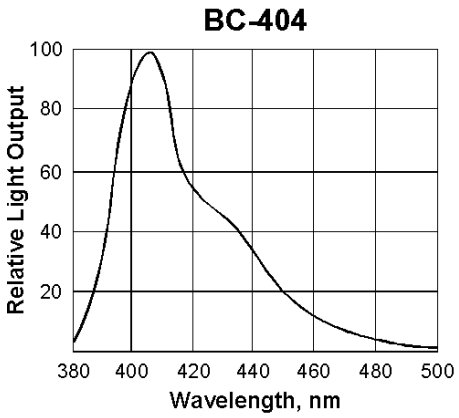

(a) Emission spectrum of the BC-404 scintillator. The peak of the emitted wavelength is at 408 nm.

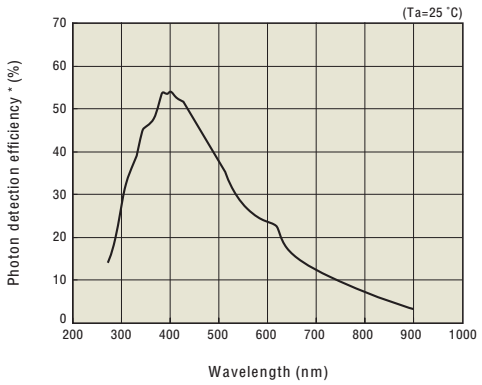

(b) Absorption spectrum of the SiPM. Peak sensitivity wavelength is at 400 nm.

Figure 4.2: Spectra of the scintillator and the SiPM [Bic10],[Ham08].

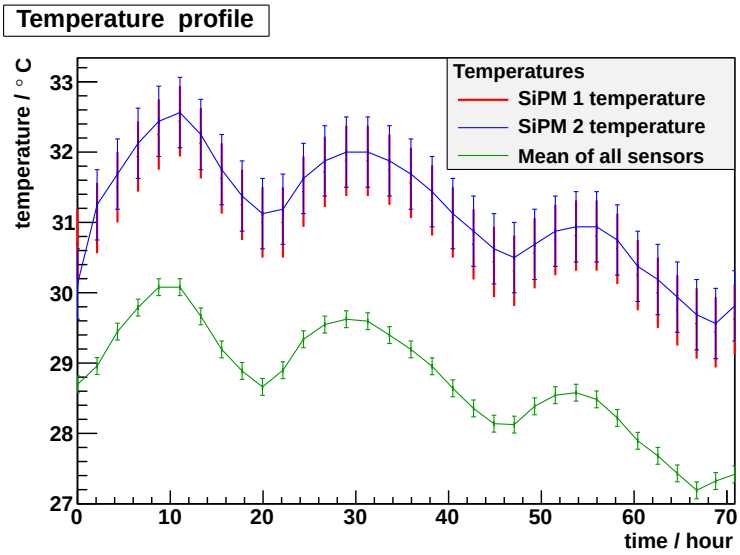

Figure 4.3: Fluctuations of the temperature at the test stand for a measurement started on July, 2nd at 11:37 am. The temperature deviates 5° to 8° from the rated SiPM temperature.

4.2 The SiPM

The used SiPM is a Hamamatsu multi pixel photon counter (MPPC) S10362-33-100C. Its dimensions are 3 mm×3 mm and its sensitive area is an array of 900 pixels with a fill factor of $\mathcal{F} = 78.5\%$. This SiPM was chosen because its PDE spectrum fits the emission spectrum of the used scintillator (see figure 4.2(b)) and the sensitive area should be large enough to produce detectable pulses from a direct scintillator read-out. The bias voltage necessary to power the SiPM slightly differs for each device and is given by the manufacturer at a rated temperature of 25 °C. It turned out that providing a constant temperature is difficult because the temperature in the laboratory deviated up to 5 °C from the rated temperature (see figure 4.3). The average bias voltage is around 71 V and to set the proper voltage for each SiPM the potentiometer on the amplifier board is used in connection with a voltmeter to determine the voltage to a precision of 10 mV.

4.3 The setup

To analyze the effect of wrappings around the scintillators there were also simulations with a wrapping of aluminium foil and Tyvek® with different reflectivities. Those two materials were simulated as a diffuse and a specular reflector. The

Table 4.1: SiPM properties

Hamamatsu S10362-33-100C	
size	3 mm×3 mm
pixel number	900
pixel size	100 µm×100 µm
peak wavelength	400 nm
rated temperature	25 °C
fill factor	78.5 %

reflectivity of aluminium foil is stated to be about 85%-95% (see [Hec01],[Hec87]). The reflectivity of Tyvek® [2] is similar to the one of aluminium foil and given as approximately 90% (see [Gic98]). Thus the simulated reflectivities of the reflectors were 98%, 95% and 80%. For a complete list of simulations see table 4.2.

Several parameters have to be provided for the simulation. One is the way the reflection is simulated. The different ways are either by simulating a reflector that lies directly on the surface of the scintillator or by simulating an air gap between the scintillator and the reflector. In the scope of this thesis for every setup an air gap of 0.15 mm was simulated. Furthermore a small gap filled with optical gel between the scintillator and the SiPM was simulated.

4.4 The simulation parameter

For a simulation run certain constellations of reflector, its reflectivity and scintillator dimensions were chosen. However a parameter was still necessary which had to be altered. Here the surface roughness of the scintillator was used. The surface roughness parameterized by the width σ_α plays a major role in reflection because if the surface is too rough, the probability for total internal reflection decreases significantly and with it the photon number reaching the SiPM. σ_α is defined as the width of the gaussian angle distribution to the surface normal. Practically this quantity may be found by analyzing a scintillator sample with the help of AFM[3]. The surface roughness for another BC-404 scintillator was determined [Pap10] to be between 2° and 4.5°. Thus, the simulation ranges from 0° to 5° for each setup with the 8 mm scintillator. For the 6 mm scintillator $\sigma_\alpha = 1°$ to $\sigma_\alpha = 3°$ are simulated because the results are planned to be used only for a raw comparison with the 8 mm scintillator. The $\sigma_\alpha = 0°$ for the 8 mm scintillator implies a perfect surface, which means that a photon that once experienced total reflection will never leave the scintillator again. To have some statistical significance the passage

[2] Tyvek® is a brand name of DuPont [Tyv10]

[3] **a**tomic **f**orce **m**icroscopy

Table 4.2: Complete list of simulated setups.

scintillator dimensions	reflector type	reflectivity
(100×100×8)mm	diffuse	98%
(100×100×8)mm	diffuse	95%
(100×100×8)mm	diffuse	80%
(100×100×8)mm	specular	98%
(100×100×8)mm	specular	95%
(100×100×8)mm	specular	80%
(100×100×8)mm	no reflector	—
(100×100×6)mm	diffuse	98%
(100×100×6)mm	diffuse	95%
(100×100×6)mm	diffuse	80%
(100×100×6)mm	specular	98%
(100×100×6)mm	specular	95%
(100×100×6)mm	specular	80%
(100×100×6)mm	no reflector	—

of 10000 muons with an energy of 2 GeV was simulated for each scintillator setup for every σ_α.

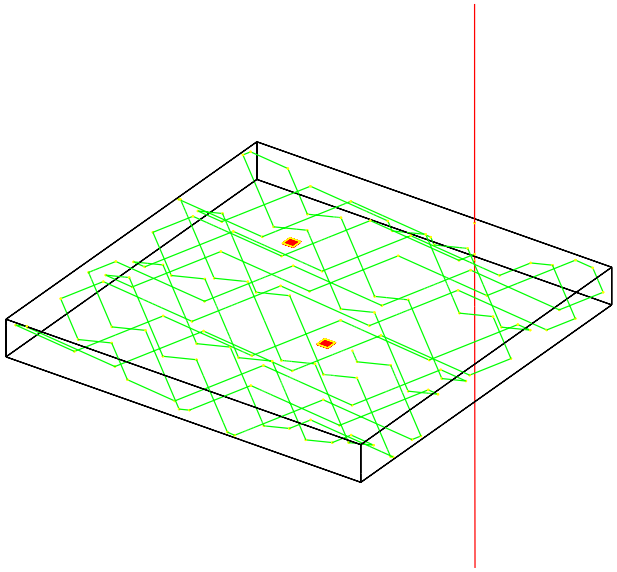

Figure 4.4: Passage of a muon through the scintillator. The red squares are the SiPMs. The red line is the trajectory of the muon. The green line is the trajectory of the generated scintillation photon.

5 Comparison of simulation and measurement

5.1 Simulation results

The first quantity that was analyzed was the number of photons at the SiPM. For this the frequency of occurrence of photon hits at the SiPM in the simulations was stored and a fit was applied to the data (see figure 5.1). The fit function

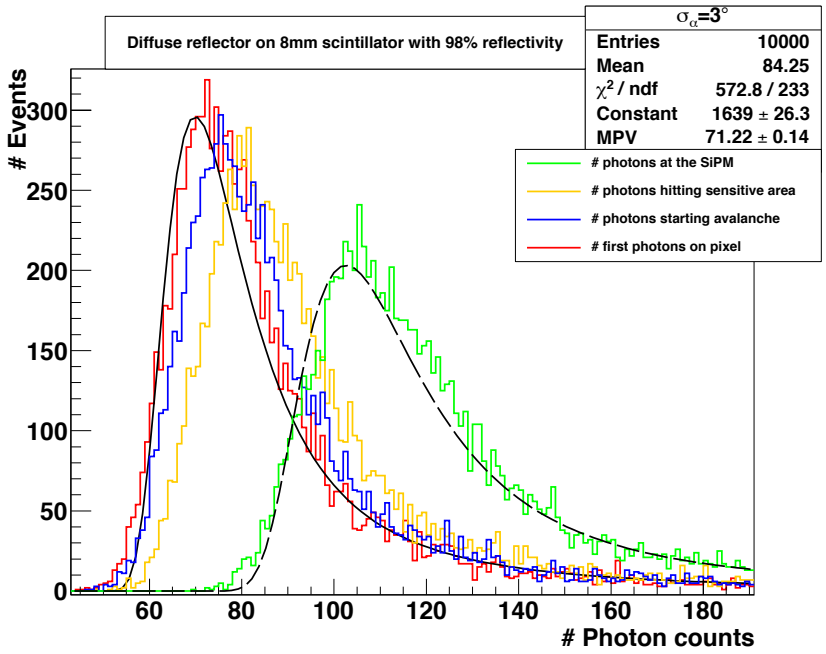

Figure 5.1: Change of the photon number for the different cut stages.

used was a landau distribution. Then three cuts were applied to the data and again fitted with a landau distribution. The first cut stage respects the fill factor of the SiPM and thus only the photons that hit the sensitive area were counted. As the start of an avalanche is a statistical effect that happens with a certain probability, in the next cut only the photons that started an avalanche were used. The last cut stage takes into account that only the first photon on a pixel that started an avalanche may be detected. Hence only the first photons on a pixel were considered. These steps were performed for every simulated setup. From the fit function the parameter called *most probable value* (MPV) was extracted for

every surface roughness and then interpreted as the number of photons fulfilling the cut stages (e.g. SiPM hit, first photon on pixel). An exception is the setup with no reflector, because in most cases no photons arrived the SiPM. That is why it was not possible to apply a landau fit to the results of the simulations with no reflector.
The first thing that can be learned from the simulation data is that the number of photons arriving at the SiPM is heavily dependent on the reflectivity of the scintillator wrapping. Even at a $\sigma_\alpha = 0°$, the number of photons that hit the SiPM decreases from nearly 130 photons at a reflectivity of 98 % to about 19 photons at a reflectivity of 80 %. For the number of photons at a certain reflectivity, it makes no difference whether the used reflector was specular or diffuse (compare tables 5.1 and 5.2). Furthermore, the photon number decreases with a higher surface roughness. Within $\sigma_\alpha = 0°$ and $\sigma_\alpha = 3°$ the number of photons hitting the SiPM first drops and then seems to level off at a certain height. This probably happens because of the reflector, which compensates that less photons experience total internal reflection. Also the fact that this effect can not be observed in simulations without reflector implies that the reflector counterbalances the surface roughness.
To analyze the effect of the reflector in combination with the surface roughness on the number of photons arriving at the SiPM, a function

$$f = a + \mathrm{e}^{-b*x+c} \tag{5.1}$$

was fitted to the MPVs for the number of photons at the SiPM (see figure 5.2). The parameter a is a constant that indicates the number of photons which would theoretically arrive at the SiPM if they were not reflected inside the scintillator. b describes the curvature of the function with the help of which it is possible to make a statement about how much the number of photons drops with higher surface roughness. Finally, c is a constant offset parameter to shift the function along the x-axis. In figure 5.2 it is shown that the fit was not applied starting at $\sigma_\alpha = 0°$. This was done so because this is a theoretical value and the fit results became worse when including it. Hence $\sigma_\alpha = 0°$ was neglected. This fit was only applied to the data from the simulations with the 8 mm scintillator because the number of degrees of freedom was not sufficient at the 6 mm scintillator. As can be seen in table 5.1, constant a of the fit function decreases with the reflectivity. This can be explained with the fact that with a poorer reflectivity of the wrapping it may less compensate the rougher surface.
An alternative attempt to fit a function to the results that would also include $\sigma_\alpha = 0°$ was made with the function

$$f_2 = a + \mathrm{e}^{-b*x+c-\frac{d}{x+g}} \tag{5.2}$$

with two additional parameters d and g. Yet it was not possible to perform this fit in the scope of this thesis because more data for surface roughnesses other

Table 5.1: Table with parameter a from the fit function for the different setups. For reasons of comparison also two MPVs for $\sigma_\alpha = 2°$ are given, as well as the mean ration of them over each surface roughness. a is a rough estimation for the 6 mm scintillator.

8 mm scintillator				
Reflector type	MPV_{detect}	MPV_{SiPM}	$\frac{MPV_{detect}}{MPV_{SiPM}}$ [%]	parameter a
Diffuse, 98%	74.9 ± 0.1	109.8 ± 0.2	68.2 ± 0.1	99.2 ± 0.3
Diffuse, 95%	41.6 ± 0.1	59.6 ± 0.1	69.3 ± 0.1	53.3 ± 0.3
Diffuse, 80%	12.3 ± 0.1	17.4 ± 0.1	72.1 ± 0.1	14.6 ± 0.3
Specular, 98%	74.9 ± 0.1	110.1 ± 0.2	68.2 ± 0.1	99.1 ± 0.3
Specular, 95%	41.7 ± 0.1	59.1 ± 0.1	69.9 ± 0.1	53.5 ± 0.3
Specular, 80%	12.5 ± 0.1	17.1 ± 0.1	71.9 ± 0.2	15.0 ± 0.3
No refl.	4.0 ± 0.6	4.6 ± 0.5	—	*(-10.4 ± 25.8)*

6 mm scintillator				
Reflector type	MPV_{detect}	MPV_{SiPM}	$\frac{MPV_{detect}}{MPV_{SiPM}}$ [%]	parameter a
Diffuse, 98%	61.6 ± 0.1	89.7 ± 0.2	68.8 ± 0.1	*60*
Diffuse, 95%	32.9 ± 0.1	46.7 ± 0.1	70.5 ± 0.2	*30*
Diffuse, 80%	9.2 ± 0.0	12.7 ± 0.1	72.7 ± 0.3	*8*
Specular, 98%	61.5 ± 0.1	89.7 ± 0.2	68.7 ± 0.1	*60*
Specular, 95%	33.0 ± 0.1	46.7 ± 0.2	70.4 ± 0.2	*30*
Specular, 80%	9.2 ± 0.0	12.7 ± 0.2	72.9 ± 0.3	*8*
No refl.	3.4 ± 0.9	1.0 ± 1.0	—	*(1)*

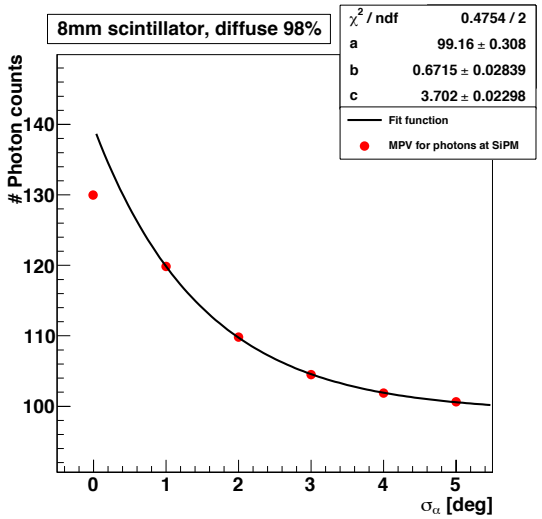

Figure 5.2: Fit to evaluate the effect of the surface roughness in combination with a reflector. The fit function is given in equation 5.1.

than the simulated ones is required to apply a fit properly. Start values for the fit parameters for an 8 mm scintillator with 98 % diffuse reflectivity are in the following orders of magnitudes:

$$a \propto 100$$
$$b \propto 1$$
$$c \propto 5$$
$$d \propto 10$$
$$g \propto 2$$

To estimate the loss of photons that may not be detected with the help of the real setup, the ratio of the MPV for first photons at a pixel and the MPV for photons hitting the SiPM was calculated (see figure 5.3). For the 8 mm scintillator it turned out that irrespectively of the used reflector the ratio of the MPVs is for 80 % reflectivity $\approx$ 72 % and decreases to $\approx$ 68 % at 98 % reflectivity. The same trend can be seen for the 6 mm scintillator, but here the ratio is $\approx$ 73 % at 80 % reflectivity and decreases to $\approx$ 69 % at 98 % reflectivity. For a list of the MPV ratios see table 5.1. The characteristic decrease of the ratio with higher reflectivities may be explained with the fact that with a greater amount of photons arriving at the SiPM because of the better reflector, the probability that a photon is the first one on a pixel diminishes. It is important to note that the results for the

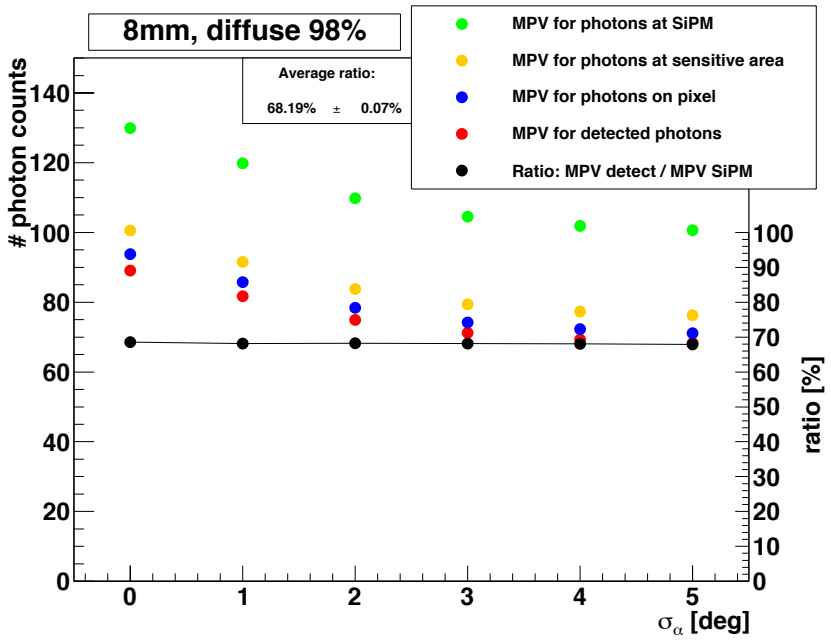

Figure 5.3: MPV values for all cut stages at different surface roughnesses and the ratio of MPV detected and MPV SiPM hit.

setups with no reflector vary around a few photons. Thus the ratio is no reasonable quantity in this case. Yet the values are given for the sake of completeness. The errors are in the order of magnitude of 100 %.
The number of photons created by a muon is linearly dependent of the scintillator thickness (see chapter 3.2). As scintillators with 8 mm and 6 mm thickness were simulated, it was possible to look at the ratio of photon counts on the SiPM for the different scintillators, which was expected to be about 75 %. In table 5.2 the results for the ratios are listed. As can be seen the ratios differ from the expectation of 75 % the more the reflectivity decreases. For a further investigation of this effect there were 3 quantities coming from the simulation regarding the process of photon creation, that were analyzed for both scintillators with Tyvek® with 98 % reflectivity.

- The first is the number of photons created per energy loss of the muon. As results came out $(8.00 \pm 0.73) \cdot 10^3 \frac{1}{\text{MeV}}$ for the 8 mm scintillator and $(8.00 \pm 0.85) \cdot 10^3 \frac{1}{\text{MeV}}$ for the 6 mm scintillator. Both values are equal within their errors, which is consistent with the theory.

- The next is the total energy loss of the muon. Here, the simulation yields an energy loss of (1.30 ± 10^{-4}) MeV for 8 mm and for 6 mm an energy loss of

Table 5.2: List of the ratios for the 8 mm scintillator and the 6 mm scintillator. The ratio is averaged over all surface roughnesses.

Diffuse	
reflectivity	ratio
98 %	(83.57 ± 0.13) %
95 %	(89.15 ± 0.18) %
80 %	(98.44 ± 0.34) %

Specular	
reflectivity	ratio
98 %	(83.66 ± 0.13) %
95 %	(89.08 ± 0.18) %
80 %	(98.23 ± 0.34) %

(0.97 ± 10^{-4}) MeV .

- Finally, the total number of created photons was analyzed. Here we gain $(1.04 \pm 10^{-4}) \cdot 10^4$ photons at the 8 mm scintillator and $(0.77 \pm 10^{-4}) \cdot 10^4$ photons at the 6 mm scintillator. Again the ratio of ≈ 75 % is in line with the expectations from the theory.

Therefore, the reason for the observed effect must lie in the geometrical setup of the detector. An approach to substantiate this could be to simulate SiPMs that are mounted on the side of the SiPM.
With respect to the comparison with the measurements the fraction of events showing photon counts below a certain threshold was calculated. The result is helpful because in the measurement a trigger needs to be set above which an event is counted to exclude the noise of the SiPM. Here, the thresholds were arrival of 40 and 50 photons. These limits were estimated, because in the measurements [Sch10] it was not possible to determine the number of photons that arrive at the SiPM. At measurements with a 1 mm×1 mm SiPM it was found that it is most improbable that more than 5 photon equivalents of charge are created by noise (see figure 3.4(b)) under normal operating conditions. As the 3 mm×3 mm SiPM has nine times as much pixels, the 40- and 50-photon thresholds were established. The fractions were calculated by integrating the photon distribution to a photon count of 40 and 50, respectively, and dividing it by the integral over the whole distribution of events (see figure 5.4). Again, the reflectivity of the wrapping plays a major role for the resulting photon counts. What can be seen for the 8 mm scintillator thickness is:

- The fraction of events, which have photon counts below the thresholds is for every surface roughness beneath one percent for a reflector with 98 % reflectivity.

- The ratio then rises for 95 % reflectivity from ≈ 3 % to ≈ 40 % for the 40-photon threshold and from ≈ 30 % to ≈ 70 % for the 50-photon threshold.

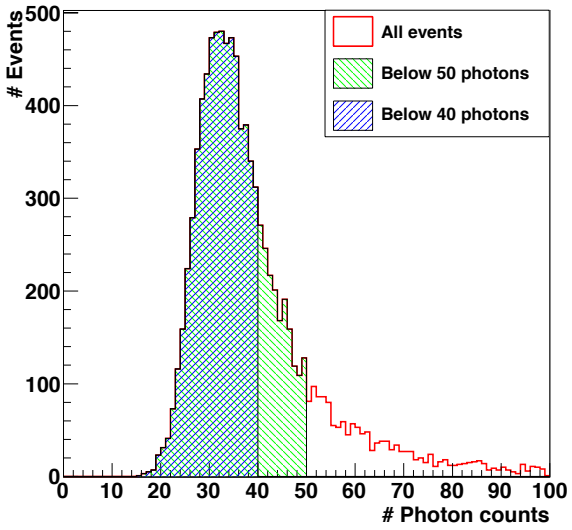

Figure 5.4: Distribution of photon numbers for the events in an 8 mm scintillator with 95 % diffuse wrapping at a surface roughness of 3°. The fractions of events below 40 and 50 photons are marked. The plot is cut off at 100 photons but the integral was calculated over the whole data.

- For the 80 %-reflector the fraction with 40 photons and below is at $\approx 93\,\% - 94\,\%$ and $\approx 95\,\% - 96\,\%$ for the 50-photon threshold.

The 6 mm scintillator shows the following behaviour:

- For a reflector with 98 % reflectivity the fraction of events below the thresholds is beneath 6 %.
- At 95 % reflectivity the fractions start at $\approx 46\,\%$ and go to $\approx 65\,\%$ for the 40-photon threshold and $\approx 75\,\%$ to $\approx 83\,\%$ for the 50-photon threshold.
- For the 80 %-reflector the scintillator shows $\approx 95\,\% - 96\,\%$ for the 40-photon threshold and $\approx 97\,\%$ for the 50-threshold.

It hast to be respected that for the 6 mm scintillator only three surface roughnesses were simulated. For simulations with no reflector, the fraction of events below 40 and 50 photons respectively was always $\approx 98\,\% - 98\,\%$. All values are listed in tables 5.3, 5.4 and 5.5. The results show that already for the reflector with 95 % reflectivity the greater part of the events shows less 50 photons on the SiPM and the fraction of events with less than 40 detected photons is rapidly rising for higher surface roughnesses. At 80 % reflectivity almost every event has less than 40 detected photons.

Table 5.3: Fractions of events below 40-photon and 50-photon threshold respectively. Results for 8 mm scintillator.

Diffuse				
Refl.	σ_α	MPV	< 40 ph.	< 50 ph.
			[‰]	[‰]
98 %	0°	89.3 ± 0.1	2.0 ± 1.4	2.0 ± 1.4
98 %	1°	82.2 ± 0.2	1.0 ± 1.0	1.0 ± 1.0
98 %	2°	74.9 ± 0.1	0 ± 0	0 ± 0
98 %	3°	71.0 ± 0.1	0 ± 0	7.0 ± 2.7
98 %	4°	69.1 ± 0.1	0 ± 0	24.2 ± 4.9
98 %	5°	68.4 ± 0.1	1.0 ± 1.0	21.1 ± 4.6
			[%]	[%]
95 %	0°	49.0 ± 0.1	3.7 ± 0.2	32.1 ± 0.6
95 %	1°	45.2 ± 0.1	10.3 ± 0.3	45.8 ± 0.7
95 %	2°	41.6 ± 0.1	21.4 ± 0.5	58.9 ± 0.8
95 %	3°	39.6 ± 0.1	29.2 ± 0.5	65.3 ± 0.8
95 %	4°	38.4 ± 0.1	34.2 ± 0.6	67.7 ± 0.8
95 %	5°	37.9 ± 0.1	36.3 ± 0.6	69.5 ± 0.8
			[%]	[%]
80 %	0°	13.8 ± 0.1	92.9 ± 1.0	95.3 ± 1.0
80 %	1°	13.1 ± 0.1	93.0 ± 1.0	95.5 ± 1.0
80 %	2°	12.3 ± 0.1	93.5 ± 1.0	95.8 ± 1.0
80 %	3°	11.8 ± 0.1	93.5 ± 1.0	95.6 ± 1.0
80 %	4°	11.4 ± 0.1	94.2 ± 1.0	96.0 ± 1.0
80 %	5°	11.3 ± 0.1	93.7 ± 1.0	95.9 ± 1.0

Specular				
Refl.	σ_α	MPV	< 40 ph.	< 50 ph.
			[‰]	[‰]
98 %	0°	89.1 ± 0.2	1.0 ± 1.0	1.0 ± 1.0
98 %	1°	81.7 ± 0.2	0 ± 0	0 ± 0
98 %	2°	74.9 ± 0.1	0 ± 0	0 ± 0
98 %	3°	71.2 ± 0.1	0 ± 0	11.1 ± 3.3
98 %	4°	69.4 ± 0.1	0 ± 0	17.1 ± 4.2
98 %	5°	68.3 ± 0.1	0 ± 0	17.1 ± 4.1
			[%]	[%]
95 %	0°	48.8 ± 0.1	4.1 ± 0.2	32.2 ± 0.6
95 %	1°	45.3 ± 0.1	10.2 ± 0.3	46.3 ± 0.7
95 %	2°	41.7 ± 0.1	21.7 ± 0.5	58.3 ± 0.8
95 %	3°	39.4 ± 0.1	30.1 ± 0.6	65.0 ± 0.8
95 %	4°	38.8 ± 0.1	33.6 ± 0.6	66.9 ± 0.8
95 %	5°	37.8 ± 0.1	38.2 ± 0.6	70.7 ± 0.8
			[%]	[%]
80 %	0°	13.7 ± 0.1	92.6 ± 1.0	95.2 ± 1.0
80 %	1°	13.2 ± 0.1	93.0 ± 1.0	95.3 ± 1.0
80 %	2°	12.5 ± 0.1	93.7 ± 1.0	95.9 ± 1.0
80 %	3°	11.8 ± 0.1	94.1 ± 1.0	96.0 ± 1.0
80 %	4°	11.4 ± 0.1	94.1 ± 1.0	96.1 ± 1.0
80 %	5°	11.3 ± 0.1	94.3 ± 1.0	96.1 ± 1.0

Table 5.4: Fractions of events below 40-photon and 50-photon threshold respectively. Results for 6 mm scintillator.

Diffuse					**Specular**				
Refl.	σ_α	MPV	< 40 ph.	< 50 ph.	Refl.	σ_α	MPV	< 40 ph.	< 50 ph.
			[‰]	[‰]				[‰]	[‰]
98 %	1°	67.1 ± 0.1	0 ± 0	37.6 ± 1.4	98 %	1°	67.4 ± 0.1	1.0 ± 1.0	37.3 ± 0.6
98 %	2°	61.6 ± 0.1	5.0 ± 2.3	228.3 ± 15.1	98 %	2°	61.5 ± 0.1	3.1 ± 1.7	245.5 ± 1.6
98 %	3°	58.5 ± 0.1	9.1 ± 3.0	597.8 ± 24.5	98 %	3°	58.7 ± 0.1	16.1 ± 4.0	513.4 ± 2.3
			[%]	[%]				[%]	[%]
95 %	1°	35.7 ± 0.1	46.9 ± 0.7	74.9 ± 0.9	95 %	1°	35.8 ± 0.1	47.7 ± 0.7	75.0 ± 0.9
95 %	2°	32.9 ± 0.1	58.7 ± 0.8	80.1 ± 0.9	95 %	2°	33.0 ± 0.1	57.6 ± 0.8	79.6 ± 0.9
95 %	3°	31.3 ± 0.1	64.3 ± 0.8	82.6 ± 0.9	95 %	3°	31.3 ± 0.1	64.0 ± 0.8	82.1 ± 0.9
			[%]	[%]				[%]	[%]
80 %	1°	9.6 ± 0.0	95.3 ± 1.0	96.7 ± 1.0	80 %	1°	9.7 ± 0.0	95.1 ± 1.0	96.7 ± 1.0
80 %	2°	9.2 ± 0.0	95.3 ± 1.0	96.9 ± 1.0	80 %	2°	9.2 ± 0.0	95.4 ± 1.0	97.0 ± 1.0
80 %	3°	8.8 ± 0.0	95.8 ± 1.0	97.1 ± 1.0	80 %	3°	8.8 ± 0.0	95.4 ± 1.0	96.8 ± 1.0

Table 5.5: Fractions of events below 40-photon and 50-photon threshold respectively. No reflector.

σ_α	MPV	< 40 ph. [%]	< 50 ph. [%]
8 mm scintillator			
1°	7.0 ± 15.3	98.3 ± 1.0	98.7 ± 1.0
2°	4.0 ± 0.6	98.1 ± 1.0	98.6 ± 1.0
3°	4.9 ± 0.4	98.4 ± 1.0	98.8 ± 1.0
6 mm scintillator			
1°	1.7 ± 1.1	98.7 ± 1.0	99.1 ± 1.0
2°	3.4 ± 0.9	98.8 ± 1.0	99.1 ± 1.0
3°	3.8 ± 0.8	98.6 ± 1.0	98.9 ± 1.0

5.1.1 Photon distribution on the SiPM

It may be also useful to look at the photon distribution on the SiPM. In figure 5.5(a) and figure 5.5(b) it can be seen that over the main part of the SiPM area the number of photon hits is uniformly distributed with the exception of the surrounding bins at the edge of the SiPM. This may be an artifact of the simulation process, where photons were refracted out of the scintillator close to the SiPM and then laterally hit the detector volume. Until now the program also counts these events and is not capable of neglecting hits from the side. Another fact which indicates that this assumption is correct is the number of the hits on the edge and at the corners. From figure 5.5(a) it is possible to roughly estimate the number of photon hits per event in the middle to approximately 0.35. The edges count 0.425 and the corners about 0.5. The edges experience 0.075 hits more per event and the corners even twice as much. This is because at the corners the SiPM has two sides susceptible to hits from the outside.

5.2 Comparison with measurements

The measurements taken in [Sch10] turned out to be hard to compare due to the incontrollable circumstances at the test stand. A stable temperature and the possibility to check the optical connection between the SiPM and the scintillator would be mandatory prerequisites for an adequate comparison. The aim to compare the number of photons that were detected could not be achieved because the noise level of the the SiPM was too high to determine a charge equivalent for a single photon. Yet the measurements show that the photon numbers at the SiPM are sufficient to create clear detection signals, which is in unison with the expectations from simulations. Another quantity that serves for comparisons is the ratio of the signal heights for the 8 mm and 6 mm scintillator. Also here the varying circumstances during measurements inhibited a proper evaluation. The ratio for one SiPM lies in the order of magnitude of 70 %, which is close to expectations, whereas the second SiPM counts only 40 %. The relatively large errors on the data leave doubt about the result. Measurements with the scintillator wrapped in felt and matt alumium showed only little signals. It stands to reason that this is because mostly the number of photons that reached the SiPMs was not high enough to cause a pulse that triggers the read-out electronics. This is in consistency with the fractions of events below a certain photon threshold for poorer reflectors. In figure 5.6 the region of possible MPVs for a certain reflectivity is given for each, the simulation and the measurements. It appears that the QDC Count MPV experienced an offset but due to the varying temperatures and with it the noise rates of the SiPMs it is not possible to draw off a global offset.

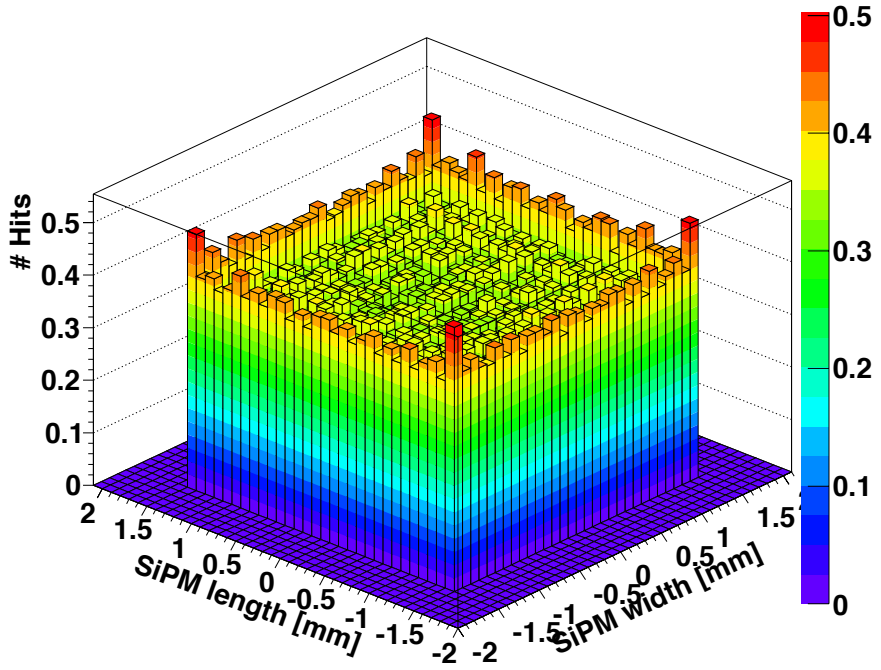

(a) Distribution of the photon hits on the SiPM for the complete SiPM area.

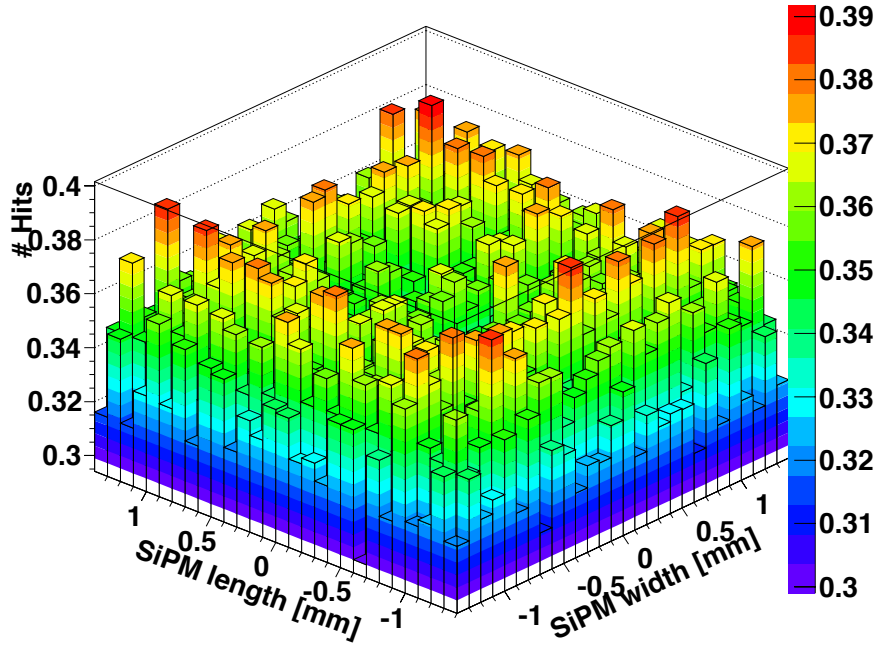

(b) Distribution of the photon hits on the SiPM without the outermost rows of bins.

Figure 5.5: Distribution of photon hits on the SiPM for a diffuse reflector with 98 % reflectivity and an assumed surface roughness of 1°. The bordering bins in (a) may be an artifact of the simulation. The bins are 100 µm×100 µm big.

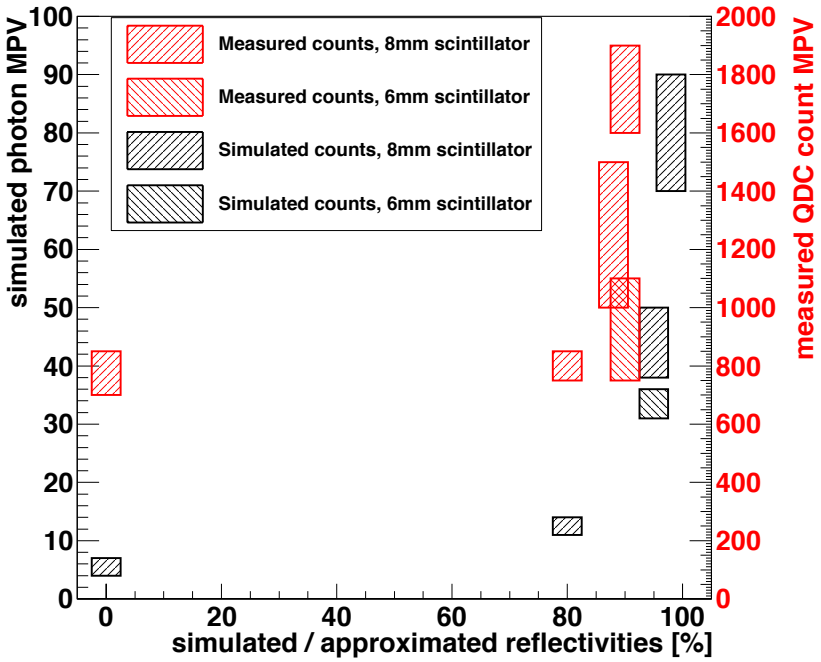

Figure 5.6: Areas of possible MPV values for measurement and simulation. The lower part for simulations at 95 % reflectivity and 90 % for measurements is for a 6 mm scintillator.

6 Conclusion and Outlook

The results of the simulations show that, looking at the reflector properties with the same reflectivities, it is of no matter, whether aluminium foil as specular reflector or Tyvek® as a diffuse reflector is used for the detector setup. However, Tyvek® may be more useful because it is more tearproof than aluminium foil and thus easier to handle. Anyway, it is necessary to wrap the scintillator with a reflector for gaining sufficient photon counts at the SiPM because it counterbalances the surface roughness of the scintillator (see figure 6.1). This effect weakens rapidly with poorer reflectivities of the wrappings. In future simulations should be surface roughnesses simulated in between the ones in this thesis to increase the amount of reading points and thus improve the fit function for the effect of the surface roughness.
The expected number of detected photons promised signals that are high enough for direct SiPM read-out and the results from [Sch10] have shown this expectation and again underlined the importance of a good reflector. However, it was not possible to make a quantitative comparison between the number of the photons in simulation and measurement. The deviations in the ratio of the photon numbers for the 6 mm scintillator and the 8 mm scintillator are not an artifact of the simulations but seem to be of geometrical nature. The results from the measurements are in one case in the order of magnitude of 70 % but the large error reduces their significance. So, the origins of this effect have to be further investigated. This may be done by simulating SiPMs mounted on the side of the scintillator and again analyzing the ratio for 6 mm and 8 mm scintillators.
With respect to the photon distribution on the SiPM in the simulations, the program has to be improved in that way, that only photon hits on one side of the sensitive volume are counted. With this it will be possible to analyze more deeply the anomaly in the photon distribution on the edges of the SiPM.
A next step in simulating further setups could be to vary the SiPM position on the scintillator. The functionality is already integrated into the program. A first outlook shows that the position of the SiPM has no impact on the photon counts but deeper analysis is mandatory.

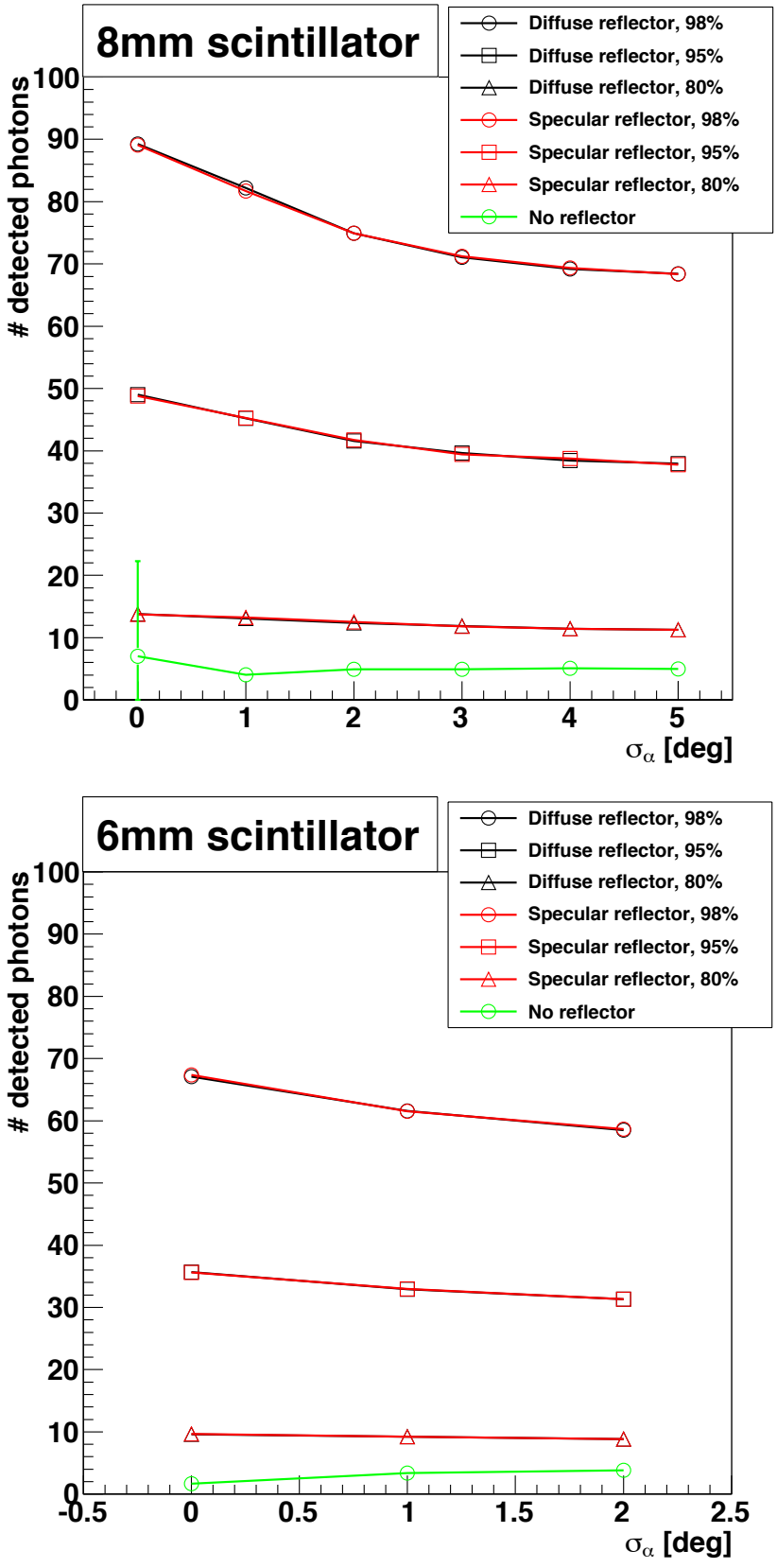

Figure 6.1: Results for the 8 mm and the 6 mm scintillator. Shown is the behaviour of the MPV in relation to different parameters.

A 3D photon distribution

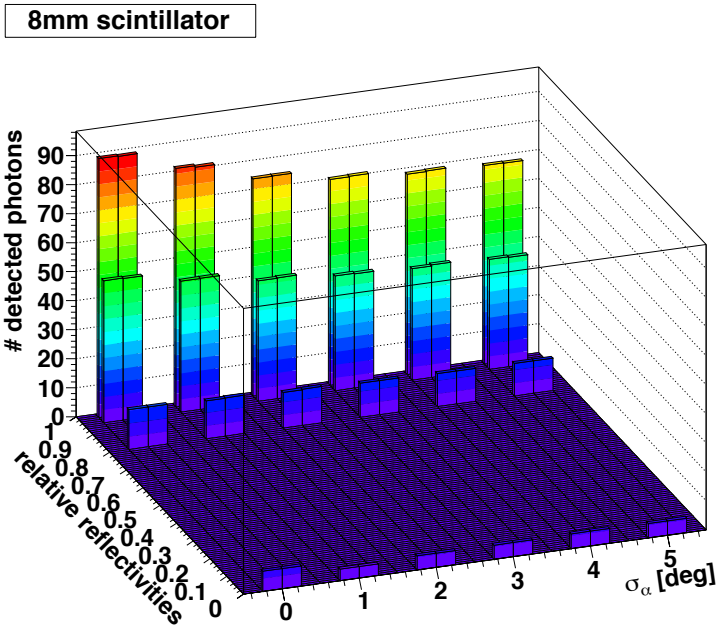

(a) Number of detected photons for the 8mm scintillator. The left bin denotes the results for the diffuse reflector, the right bin for the specular reflector. At a relative reflectivity of 0 only a single simulation with no reflector was performed.

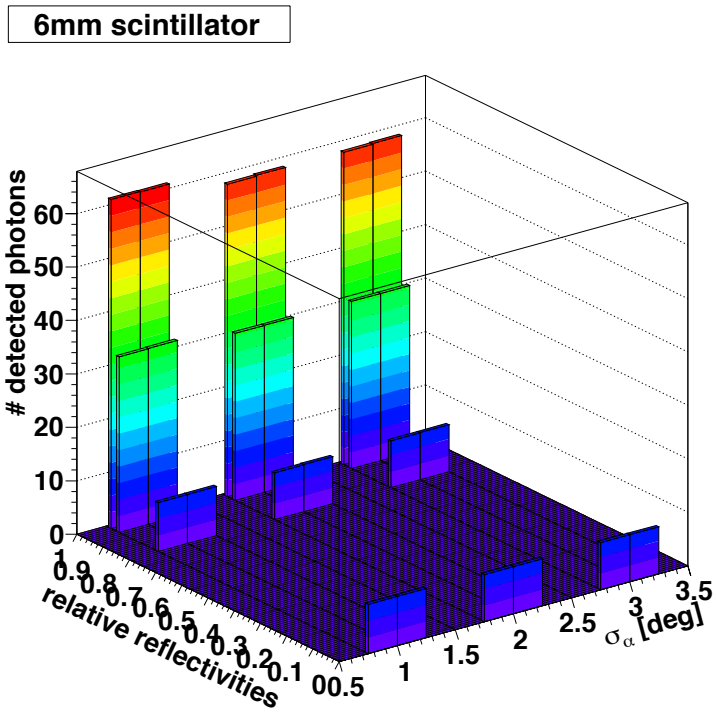

(b) Number of detected photons for the 6mm scintillator. The left bin denotes the results for the diffuse reflector, the right bin for the specular reflector. At a relative reflectivity of 0 only a single simulation with no reflector was performed.

Figure A.1: Number of detected photons for the 6mm and 8mm scintillator.

Bibliography

[Bic10] Bicron. *BC-404 Datasheet.* http://www.phys.ufl.edu/courses/phy4803L/group_I/muon/bicron_bc400-416.pdf, June 2010.

[CDF95] *Observation of Top Quark production in p anti-p Collisions with the Collider Detector at Fermilab.* Phys. Rev. Lett. 74, 2626. The CDF Collaboration, 1995.

[CMS10a] *The CMS experiment at the CERN LHC.* CMS Collaboration, 2010.

[CMS10b] CMS Webpage. http://cms.web.cern.ch/cms/Media/Images/Detector/DetectorDrawings/index.html, May 2010.

[Eva08] Philip Bryant; Lyndon Evans. *LHC Machine.* European Organization for Nuclear Research, 2008.

[GEA10] Geant4 user documentation. http://geant4.web.cern.ch/geant4/UserDocumentation/UsersGuides/ForApplicationDeveloper/html/index.html, June 2010.

[Gia05] F. Gianotti. *Physics potential and experimental challenges of the LHC luminosity upgrade.* http://cmsdoc.cern.ch/cms/electronics/html/elec_web/docs/SLHCf.pdf, January 2005.

[Gic98] Justus Ogwoka Gichaba. *Measurements of TYVEK Reflective Properties for the Pierre Auger Project.* The Universitiy of Mississippi, August 1998.

[Gob] Saint Gobain. *BC-404 Datasheet.* http://www.detectors.saint-gobain.com/uploadedFiles/SGdetectors/Documents/Product_Data_Sheets/BC400-404-408-412-416-Data-Sheet.pdf.

[Gro08] Particle Data Group. *Particle Data Booklet.* July 2008.

[Gru08] Boris A. Shwartz; Claus Grupen. *Particle Detectors.* Cambridge University Press, 2. edition, 2008.

[Ham08] Hamamatsu. *Multi Pixel Photon Counter. Brochure on MPPCs.* January 2008.

[Hec87] Eugene Hecht. *Optics*. Addison-Wesley Publishing Company, 2. edition edition, 1987.

[Hec01] Eugene Hecht. *Optik*. Oldenbourg Verlag München Wien, 3. edition edition, 2001.

[LHC10] CERN Webpage. http://cdsweb.cern.ch/record/841555/files/lhc-pho-1998-349.jpg, June 2010.

[Lut07] Gerhard Lutz. *Semiconductor Radiation Detectors*. Springer, 2nd printing of 1st edition, 2007.

[Mar06] Brian R. Martin. *Nuclear and Particle Physics*. John Wiley & Sons, Ltd, 2006.

[Mon07] A. Montanari. *Muon Trigger Upgrade at SLHC: Muon Track fast Tag*. I.N.F.N. Italy, October 2007.

[Pap10] Paul Papacz. *Optimisation of the Particle Detection Efficiency for Scintillation Detectors with SiPM Readout*. March 2010.

[Ren09] Dieter Renker. *Advances in solid state photon detectors*. 2009.

[Sch10] Florian Scheuch. *Measurements of a detector prototype with direct SiPM read-out and comparison with simulations*. July 2010.

[Ser05] Clement Moses; Curt Moyer; Raymond Serway. *Modern Physics*. Thomson Brooks/Cole, 3 edition, 2005.

[Tyv10] Tyvek handbook. PDF: http://www2.dupont.com/Tyvek/en_US/assets/downloads/tyvek_handbook.pdf, July 2010.

Acknowledgements

An erster Stelle möchte ich Herrn Professor Hebbeker danken, da er mir erst die Möglichkeit gab, diese Arbeit in diesem Institut anzufertigen. Als nächstes gebührt großer Dank Markus Merschmeyer und Paul Papacz, die beide unermüdlich und mit großer Geduld bei dieser Arbeit zur Seite standen und bemüht waren, jede Frage zu beantworten und Tipps zu geben. Ohne euch hätte ich diese Arbeit bestimmt nicht so auf die Beine stellen können. Mein Dank gilt auch Florian Scheuch, dessen Arbeit auch für die Anfertigung meiner Arbeit wichtig war. Danken möchte ich auch dem gesamten physikalischen Institut 3A, deren Mitarbeiter mich sehr herzlich aufgenommen haben und mir das Gefühl gaben, ein vollwertiges Mitglied in diesem Institut zu sein. Auch meinen Eltern und meiner Familie danke ich, denn ohne ihre Unterstützung wäre mein Studium überhaupt nicht möglich. Auch meiner Freundin, Waltraud, möchte ich danken, die während der Zeit, in der ich diese Arbeit angefertigt habe, sehr viel auf mich verzichten musste ($\heartsuit \leftarrow$ für Dich, als Entschädigung!). Sigrid Kliem und Marc Richter möchte dafür danken, dass sie einen Blick über meine Arbeit geworfen haben und einige Ratschläge parat hatten, wie man diese Arbeit verbessern könne. Als letztes möchte ich allen anderen danken, die mich bei der Anfertigung dieser Arbeit unterstützt haben, und die ich namentlich nicht alle erwähnen kann.

Erklärung

Ich versichere, diese Arbeit selbstständig verfasst und keine anderen als die angegebenen Hilfsmittel und Quellen benutzt zu haben.
Aachen, 03. August 2010

Andreas Künsken